Supplementary materials for "Experimental demonstration of quantum effects in the operation of microscopic heat engines"

J. Klatzow,[1,*] J. N. Becker,[1] P. M. Ledingham,[1] C. Weinzetl,[1] K.T. Kaczmarek,[1]
D. J. Saunders,[1] J. Nunn,[2] I. A. Walmsley,[1,†] R. Uzdin,[3] and E. Poem[4,‡]

[1]*Clarendon Laboratory, University of Oxford,*
Parks Road, Oxford OX1 3PU, United Kingdom
[2]*Centre for Photonics and Photonic Materials,*
Department of Physics, University of Bath,
Claverton Down, Bath BA2 7AY, United Kingdom
[3]*Fritz Haber Research Center for Molecular Dynamics,*
Hebrew University of Jerusalem, Jerusalem 9190401, Israel
[4]*Department of Physics of Complex Systems,*
Weizmann Institute of Science, Rehovot 7610001, Israel

[*] email: james.klatzow@physics.ox.ac.uk.
[†] email: ian.walmsley@physics.ox.ac.uk.
[‡] email: eilon.poem@weizmann.ac.il.

CONTENTS

S1. Quantum Heat Engines – brief introduction 3

S2. Sample preparation 4

S3. The experimental setup 4

S4. Spectroscopy and calibrations 6

S5. Rate equation model 8

S6. Emulation of a thermal action 13

S7. Engine performance calculations 18

S8. Derivation of the stochastic bound 20

S9. Quantum Heat Engine Equivalence 21

S10. Linking the fluorescence to the engine work output 23

S11. Uncertainty Analysis 27

References 27

S1. QUANTUM HEAT ENGINES – BRIEF INTRODUCTION

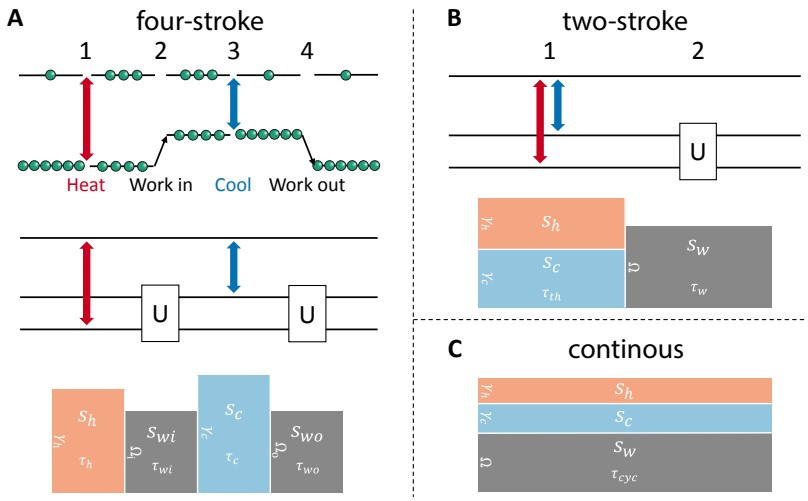

FIG. S1: **Quantum heat engine schematics. a,** An example of a four-stroke engine. Top: The classical case of two levels with a variable energy gap. Middle: A generalization by embedding the operation into three constant levels with general unitary transformations. Bottom: schematic description. The gray rectangles represent the unitary (work-extracting) operations, while the orange (light blue) rectangle represents coupling to a hot (cold) thermal bath. The horizontal dimension represents time, while the vertical represents coupling rate. The area of each rectangle is the stroke action (in units of $\hbar$). **b,** The two-stroke engine. Top: three-level embedding. Bottom: Schematic description. **c,** Schematic description of the continuous engine. All the three examples presented here have the same coherent and thermal actions per cycle.

Here we give a brief introduction to the cycle structures of the various types of quantum heat engines, the multi-level embedding, and stochastic engines, which are illustrated in Fig. S1. First consider the case, illustrated in the top panel of (**a**), of a stochastic engine, which consists of a two level system whose energy levels can be varied. Populations are transferred by coupling these levels hot and cold baths, and work is done by adiabatically shifting the levels after the thermal couplings, without generating coherence. It can be shown [1] that this scheme can be embedded in a three level system with the shift operations exchanged for complete swap operations between the lower two levels, as shown in the middle panel of (**a**) with U = swap. Note that the hot and cold

levels now couple the upper level to the lower and middle levels respectively. The general quantum case of this embedding involves replacing the swap operations with general unitary operations; here the stochastic case corresponds to a π pulse. The bottom panel of (**a**) is a schematic representation of the cycle structure, where gray represents the unitary stroke, red the coupling to the hot bath, and blue the cold bath; the horizontal scale represents the time and the vertical represents the coupling strength, so that the area of each block represents the contribution to the action (in units of $\hbar$). Fig **b** shows the equivalent embedding and schematic diagrams for the two-stroke engine, in which the thermal stroke consists of a joint coupling of both hot and cold baths, which is then followed by a unitary stroke. Finally, Fig **c,** shows the schematic for the continuous engine which simply consists of continuous and constant couplings to both thermal baths and the work reservoir.

S2. SAMPLE PREPARATION

A type Ib high-pressure-high-temperature $3\times3\times0.5$ mm, (100) diamond slab (Element-Six) with an initial nitrogen concentration of $\sim$200 ppm was electron irradiated (10^{18} cm^{-2}) and then annealed (950°C, 2.5 hours), to form a dense ($\sim10^{18}$ cm^{-3}) ensemble of NV$^-$ centres. The orientations of the centres are randomly distributed between all the $\langle 111\rangle$ directions. However, the microwave (MW) driving is resonant only with the centres oriented parallel to the magnetic field, and thus only these centres ($\sim$25% of all centres) produce the work.

S3. THE EXPERIMENTAL SETUP

The experimental system is schematically presented in Fig. S2(a). The diamond sample was placed between two permanent magnets aligned along the $[111]$ direction. A solid-state continuous-wave laser at 532 nm was focused inside the diamond sample to a spot of (nominally) 2.2 μm in diameter by a long-working-distance objective lens (NA=0.29). An acousto-optic modulator (AOM) was used for the intensity modulation of the laser-light reaching the sample. In addition, an AC magnetic field was applied to the sample by a broad-band MW strip-line waveguide embedded in the sample holder. Just below the sample, the strip-line was narrowed down to a width of 300 μm, in order for the applied field to be both strong enough and uniform across the active

volume. A photograph of the sample on the MW waveguide is presented in Fig. S2(b).

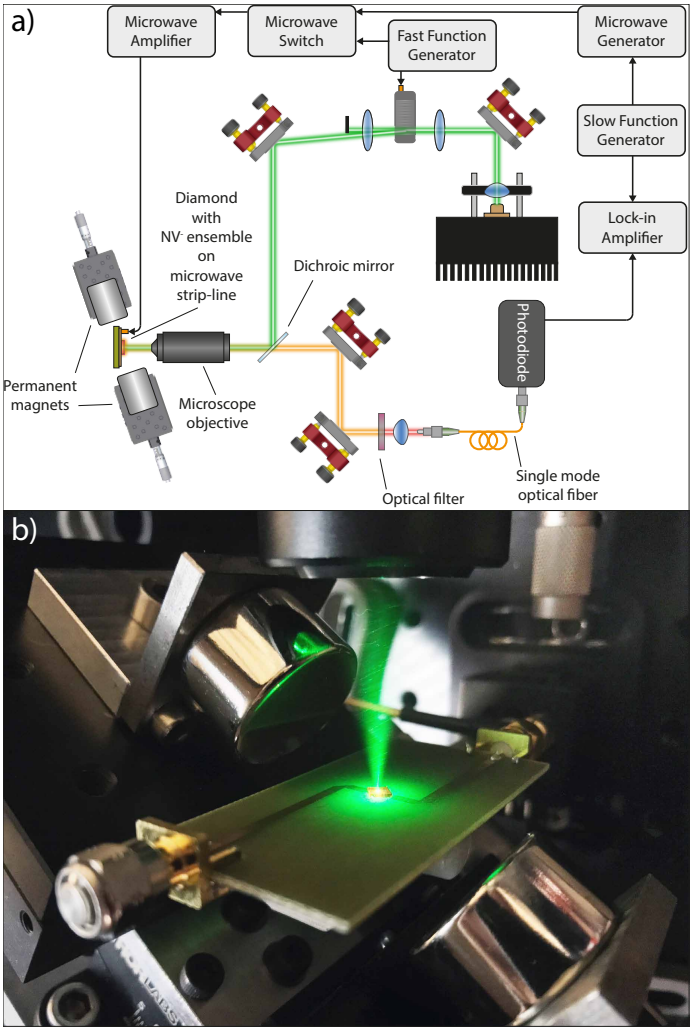

FIG. S2: Experimental setup. (a) Schematic description. The fast function generator, driving the AOM and the MW switch, allows for the implementation of the two-stroke engine. Using slow amplitude modulation of the MW and lock-in detection allows for direct measurement of the net change in fluorescence induced by the operation of the engine. (b) A photograph showing the diamond sample on the MW waveguide between the two magnets. The diamond is glowing red while the green illumination is on.

A fast MW switch (MS) between the MW generator and the MW amplifier was used for the amplitude modulation of the applied MWs. The MS and the AOM had switching times of 1.5 ns

and 12 ns, respectively, and were both simultaneously driven at $\sim$MHz rates by a fast function generator.

The fluorescence emitted from the diamond was collected by the objective lens and was imaged with a $\times 10$ magnification on a single-mode optical fibre. This confocal geometry ensures the collection of light only from the central part of the laser spot, where the optical excitation rate is maximal and approximately uniform. The collected light was then detected by an avalanche photo diode operating in the linear regime.

To efficiently detect the change in fluorescence due to the operation of the engine, that is, due to the MW driving, lock-in detection was used, where the output of the MW generator was amplitude-modulated by a $\sim$100 Hz square wave, much slower than the repetition rates of the engine, and a lock-in amplifier was locked to this slow modulation.

S4. SPECTROSCOPY AND CALIBRATIONS

Here we describe the initial characterization of the experimental setup, and the calibration of its control parameters.

First, the distance between the magnets, as well as their mean position with respect to the sample were adjusted, such that the resonance frequency was $2\pi \cdot 2600$ MHz. During this process, we observed an anti-crossing between $|0\rangle$ and $|-1\rangle$. The angle of the magnetic field was adjusted to minimise the gap at the anti-crossing point, from which we were able to infer the field angle relative to the NV axis. In our case, the angle was determined to be 0.6°. The transition was found to be inhomogeneously broadened with minimal full-width at half maximum of $2\pi \cdot (7 \pm 0.7)$ MHz, determined by a Gaussian fit. This implies a maximal ensemble coherence time ($1/e$) of 75 ± 7.5 ns. This was also confirmed by directly measuring the decoherence time using Ramsay interferometry, which yielded a similar result. Then, by measuring the change in fluorescence as a function of the MW pulse length, the Rabi-frequency was measured for different MW intensities. It was found that the ratio between the Rabi frequency and the square root of the applied MW power (after the amplifier) was $2\pi \cdot (244 \pm 2)$ kHz/$\sqrt{\text{mW}}$. The maximum MW power available after the amplifier was 3000 mW, such that Rabi frequencies up to $2\pi \times 13.3$ MHz could be applied.

To determine the dependence of the optical excitation rate, Γ, on the laser power in our set-up,

we scanned the laser power whilst measuring the total fluorescence. As can be seen in Fig. S3, one obtains a curve which is linear for small laser powers, but then deviates from linear dependence. We used a rate equation model (see Sec. S5 below) to fit to the data using the ratio between the laser power and Γ as a fitting parameter (together with the overall coefficient for the fluorescence). All the other parameters are known from previous, independent measurements [2]. The obtained ratio between Γ and the laser power measured before the objective lens was $r = 436 \pm 25$ kHz/mW. Note that this number depends on the position in the sample of the focus of the beam, most probably due to absorption in the sample. The maximum optical power available (as measured before the objective lens) was 4.0 mW (maximal optical excitation rate of 1.74 MHz), where optical power used in the experiments presented in the main text was 1.75 mW ($\Gamma = 0.76$ MHz).

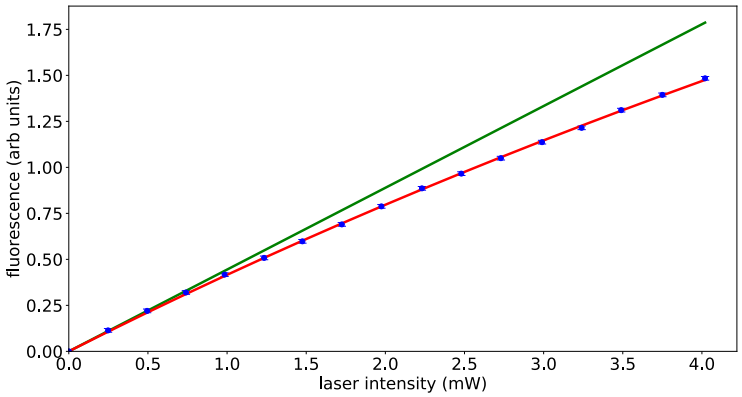

FIG. S3: Measured (symbols) and fitted (red line) fluorescence saturation curves. Using the rate equation model described in Sec. S5, the ratio between the optical excitation rate, Γ, on the light intensity, I_{laser}, was determined. The green line is the tangent at zero laser intensity, showing that the saturation curve significantly deviates from linear behaviour.

One can compare the measured r with a simple calculation using the known absorption cross-section of an NV$^-$ centre at 532 nm ($\varsigma = (3.1 \pm 0.8) \times 10^{-17}$ cm^2 [3]), $r = \varsigma/(A\varepsilon_L)$, where A is the laser spot area and ε_L is the energy of one laser photon. When taking into account the measured transmission of the objective lens (81%), the Fresnel transmission of the diamond surface (83%), and absorption due to propagation to the middle of the sample through a dense ensemble of 10^{18} cm^{-3} NV$^-$ centers (45% transmission), one finds that the focal spot diameter that yields the measured value of r is 2.7 ± 0.4 μm, in good agreement with the nominal value of 2.2 μm

predicted for a perfect 0.29 NA objective lens. The small discrepancy might be due to deviations of the exact position of the focal spot or the exact NV^- density from the estimated values used above, or due to aberrations.

S5. RATE EQUATION MODEL

The spin-state-dependent fluorescence intensity exhibited by NV^- centres [4] was a part of our initial motivation for using NV^- centres to implement a quantum heat engine. In this section we show how this property, quantified using a rate equation model, allows us to take all the measurements required for the experiment.

The fluorescence spectrum for the optical excitation intensities used in this experiment contained less than 1% neutral NV (NV^0) emission. Furthermore, the charging rates for these excitation intensities are expected to be on the order of $\sim 1\mu$s [5], longer than all the other characteristic times in the system (see below). We therefore neglect optical charging effects (transitions from NV^- to NV^0 and back), and focus on the dynamics within the NV^- states.

The NV^- centre consists of a ground state spin triplet, denoted by ${}^3A_2$, two excited spin triplets, ${}^3E$, as well as three intermediate singlets, ${}^1E_{1,2}$ and ${}^1A$. Of the various interactions that lift the degeneracy of the sub-levels in the ground and excited states, orbital averaging at room temperature results in only the axial spin-spin interaction remaining [6]; this allows us to treat the two excited state triplets as a single triplet.

Illuminating the NV-centre with 532nm light excites it into the phonon sideband, from which it rapidly decays via spin-preserving phonon transitions into the ^{3}E manifold. These fast phonon decays (< 1 ps) ensure that the whole process is both incoherent and Markovian, which are important requirements for the thermal action [1].

Additionally, the upper of the three singlets, ${}^1A_1$, decays directly into the lower pair, ${}^1E$, and has so short a lifetime (< 1 ns) as to allow us to treat the three singlets as an effective single state . A diagram of this structure, together with the allowed transitions is shown in Fig. S4.

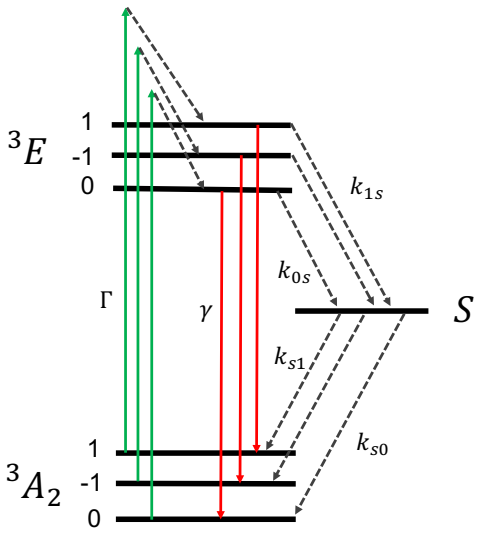

FIG. S4: The simplified NV^- level system used for the calculations. Horizontal lines represent levels, solid arrows represent allowed optical transitions, and dashed arrows represent non-optical transitions. G is the ground-state triplet, E represents the excited-state triplet, and S represents the three singlets (see text).

We define the rate matrix,$\mathcal{R}$, to be that whose elements, $\mathcal{R}_{ij}$, are rates of transfer from the i^{th} to j^{th} level. Then, in the basis $\{G_0, G_{-1}, G_1, E_0, E_{-1}, E_1, S\}$ (see Fig. S4), $\mathcal{R}$ is given by,

$$\mathcal{R} = \begin{bmatrix} 0_{3\times3} & \Gamma\,\mathbb{I}_{3\times3} & 0_{3\times1} \\ \gamma\,\mathbb{I}_{3\times3} & 0_{3\times3} & v_{3\times1} \\ u_{1\times3} & 0_{1\times3} & 0_{1\times1} \end{bmatrix}.$$

Here each of the matrix elements represents a block (with size given by the subscript), the vectors v and u are given respectively by $(k_{0s}\ k_{1s}\ k_{1s})^T$ and $\left(k_{s0}\ \frac{1}{2}k_{s1}\ \frac{1}{2}k_{s1}\right)$, and the known [2] rate constants are given in Table S1. Note that these decay rates do not depend on the optical or the microwave driving of the system, as the relevant coupling rates, and therefore any driving-induced level shifts, are much smaller than the level spacings.

TABLE S1: Spontaneous decay rates between NV levels used in the analysis. Taken from Ref. 2 (averaged over all NV^- orientations).

	rate (MHz)
γ	65.9 ± 1.9
k_{1s}	53.3 ± 2.5
k_{0s}	7.9 ± 1.4
k_{s0}	0.98 ± 0.31
k_{s1}	0.73 ± 0.11

Under optical excitation the system will evolve according to,

$$\partial_t \sigma = M\sigma,$$

where σ represents the populations in vector form and the matrix M is given in terms of the rate matrix, $\mathcal{R}$, by,

$$M_{ij} = \mathcal{R}_{ji} - \delta_{ij} \sum_k \mathcal{R}_{ik}. \tag{S1}$$

The rate matrix presented above is for the zero field case; when working under a magnetic field we need to determine the transformed version of $\mathcal{R}$, and use this to calculate M. The Hamiltonians for the ground and excited state manifolds are given by,

$$\mathcal{H}_{\text{gs}} = D_{gs} S_z^2 + g\mu_B \vec{B} \cdot \vec{S},$$
$$\mathcal{H}_{\text{es}} = D_{es} S_z^2 + g\mu_B \vec{B} \cdot \vec{S},$$

where $\vec{B}$ is the magnetic field, $\vec{S}$ is the spin vector operator, $\vec{S} = (S_x, S_y, S_z)$, and all the other parameters are listed in Table S2.

TABLE S2: Parameters of the NV^- spin Hamiltonians. Taken from Ref. 7.

Parameter name	Symbol	Value	Units
Lande g factor	g	2.00	-
Bohr magneton	μ_B	$2\pi \times 14.0$	GHz/T
Ground state spin-spin int.	D_{gs}	$2\pi \times 2.87/3$	GHz
Excited state spin-spin int.	D_{es}	$2\pi \times 1.44/3$	GHz

The resulting singlet and ground-state energy levels vs. the magnetic field, for an off-axis angle of $0.6°$, are shown in Fig. S5.

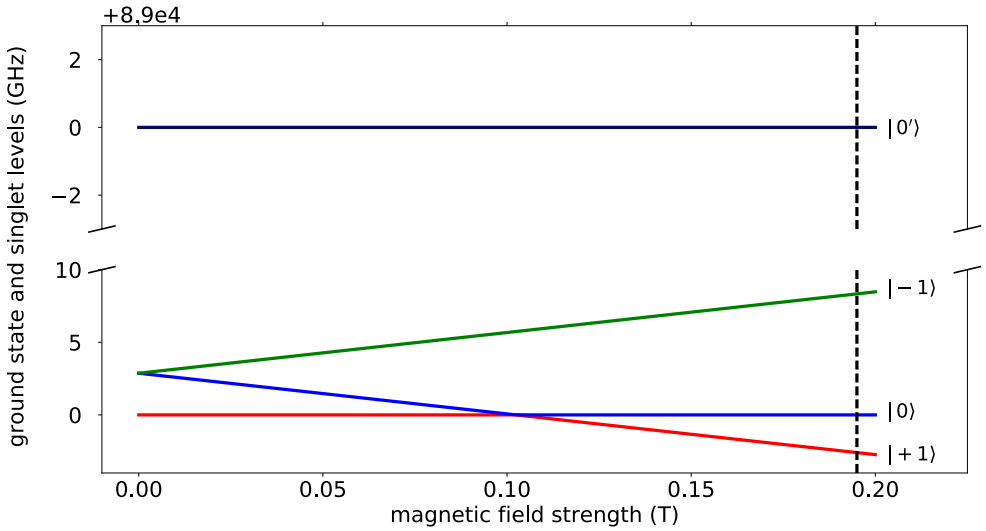

FIG. S5: Singlet and ground state energy levels as a function of magnetic field strength $0.6°$ off the NV^- symmetry axis. The dashed vertical line indicates the field strength used in the experiment.

Let the unitary transformation between the zero field and final energy eigenstate be denoted by U. The contribution of state $|k\rangle$ to the population of the transformed state $\left|\tilde{i}\right\rangle$ is $|U_{ik}|^2$. Elements in the transformed rate matrix are then given by a sum over the zero-field rates, weighed by these factors:

$$\mathcal{R}_{ij} \to \sum_{k,l} |U_{ik}|^2 |U_{jl}|^2 \mathcal{R}_{kl} \implies \mathcal{R} \to |U|^2 \mathcal{R} \left|U^T\right|^2,$$

where $|U|^2$ denotes the element-wise absolute square. In Fig. S6 (a) we use the matrix obtained in this manner to calculate the steady state populations of the NV centre as a function of axial magnetic field strength, for the optical excitation rate used in the experiment. The sharp changes at $\sim 0.05T$ and $\sim 0.1T$ correspond to anti-crossings in the excited and ground states respectively. Fig. S6 (b) shows the corresponding effective temperatures between the levels (as calculated using the Boltzmann factor and the known energy splittings between the ground-state triplet and the metastable singlet of (89 ± 10) THz [8]).

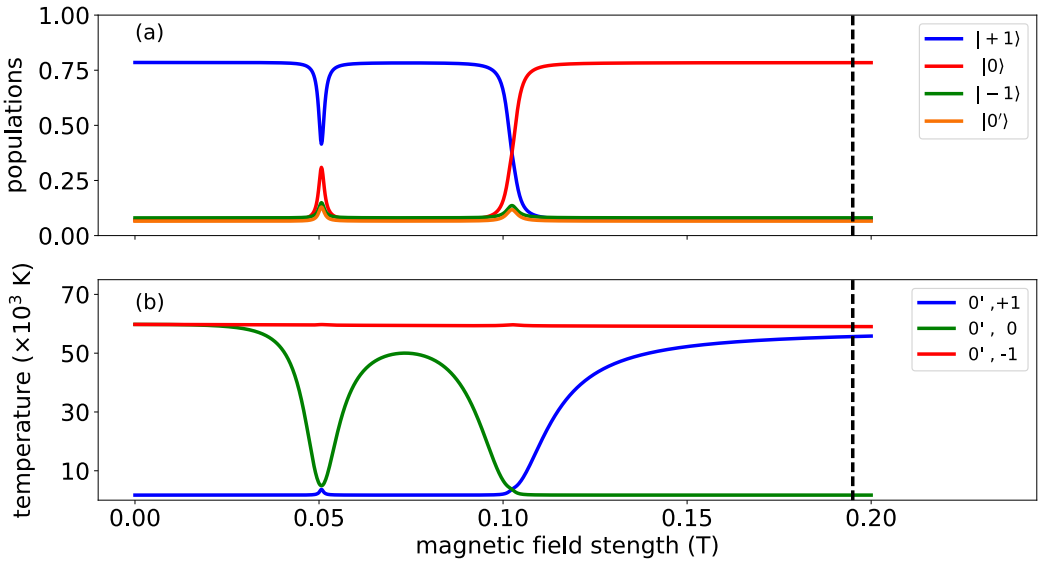

FIG. S6: Steady state populations (a) and effective temperatures of the thermal reservoirs (b) as a function of the magnetic field, for the optical excitation rate used in the experiment (0.76 MHz). The legend refers to the spin state of the level at the magnetic field used in the experiment (indicated by the vertical dashed line). The ground-singlet ($^3A_2 - ^1E$) splitting used for the temperature calculation is (89 ± 10) THz [8].

S6. EMULATION OF A THERMAL ACTION

We now show that the optical cycle in the NV^- centre does indeed emulate a thermal interaction. The intuitive idea is that the optical cycle transfers population from $|\pm 1\rangle$ to $|0\rangle$ in the ground state manifold. We will formalise this and show precisely how to obtain the emulated action. The goal is to find a projection operator, $\mathcal{P}$, on the set of population vectors, together with a reduced evolution operator L, which satisfies the requirements for a thermal evolution operator, such that the following condition is satisfied:

$$e^{Lt}\left(\mathcal{P}\sigma\right) = \mathcal{P}\left(e^{Mt}\sigma\right) \tag{S2}$$

This condition is a statement that the thermal operator L should describe the time evolution of the reduced state, when the evolution of the whole system is generated by the optical matrix M. The approach we take is to treat our system as an effective 4 level system, consisting of the ground states together with the singlet, $\sigma_{red} = [\ g_0\ ,\ g_1\ ,\ g_{-1}\ ,\ s\ ]$, which is described by the projection,

$$\mathcal{P} = \begin{bmatrix} 1 & 0 & 0 & 0 & 0 & 0 & 0 \\ 0 & 1 & 0 & 0 & 0 & 0 & 0 \\ 0 & 0 & 1 & 0 & 0 & 0 & 0 \\ 0 & 0 & 0 & 0 & 0 & 0 & 1 \end{bmatrix}.$$

This is a justifiable choice if we can find the operator L which satisfies the requirements for a thermal operator ($L_{ij} \geq 0$ for $i \neq j$, $L_{ij} \leq 0$ for $i = j$, and $L_{ij} \leq L_{ji}$ for $i > j$) and Eq. S2 to a good approximation. This will be done through an eigen-analysis of the matrix M. Using Eq. S1, it can be shown that M is given by,

$$M = \begin{bmatrix} -\Gamma\, \mathbb{I}_{3\times 3} & \gamma\, \mathbb{I}_{3\times 3} & u \\ \Gamma\, \mathbb{I}_{3\times 3} & -\left(\gamma\, \mathbb{I}_{3\times 3} + V\right) & 0_{3\times 1} \\ 0_{1\times 3} & v & -\sum_{i=1}^{3} u_i \end{bmatrix},$$

where V is a diagonal matrix with the elements of v on its diagonal.

The remaining eigenvectors and values can be found using perturbation theory. The perturbative expansion is taken about a value in the middle of the range that we use in the experiment,

specifically $\Gamma = 0.5$ MHz. The zeroth order eigenvalues are given (in units of MHz) by and have corresponding eigenvectors in the basis $\{G_0, G_{-1}, G_1, E_0, E_{-1}, E_1, S\}$,

$$\lambda^{(0)} = [\, 0.0\ ,\ -0.15\ ,\ -0.22\ ,\ -1.84\ ,\ -74.28\ ,\ -119.47\ ,\ -119.48\,]$$

$$\sigma^{(0)} = \begin{bmatrix} 0.99 & 0.84 & 0.00 & -0.46 & -0.66 & 0.00 & 0.00 \\ 0.09 & -0.38 & 0.71 & -0.19 & 0.00 & -0.10 & 0.45 \\ 0.09 & -0.38 & -0.71 & -0.19 & 0.00 & -0.43 & -0.11 \\ 0.01 & 0.01 & 0.00 & 0.00 & 0.74 & 0.00 & 0.00 \\ 0.00 & 0.00 & 0.00 & 0.00 & 0.00 & 0.18 & -0.82 \\ 0.00 & 0.00 & 0.00 & 0.00 & 0.00 & 0.77 & 0.19 \\ 0.06 & -0.08 & 0.00 & 0.85 & -0.08 & -0.43 & 0.29 \end{bmatrix}$$

We can split these eigenvectors (and their eigenvalues) into two groups as follows: the first four eigenvectors are those which describe the changes in the 3 ground states and the singlet and for which the components corresponding to the excited states are at least an order of magnitude smaller than the other components; the other three eigenvectors have large components corresponding to the excited state triplets. This partitioning also splits the eigenvalues according to their magnitude, with the last three at least an order of magnitude greater than the first four. Note too that, if we restrict our attention to the ground state triplet together with the singlet, then the first four form a linearly independent set spanning these states. Therefore, if the system has little population in its excited states, the coefficients of the final three eigenvectors will be correspondingly small and we can write such a state in terms of the first set of eigenvectors to a good approximation. By considering the first and second order perturbative corrections, it can be shown that this is true for all Γ used in the experiment ($|\Delta\Gamma| \leq 0.5$ MHz, where $\Delta\Gamma \equiv \Gamma - 0.5$ MHz). We now return to the problem of finding L. Consider Eq. S2 – note that this condition holds if the following holds:

$$[L\mathcal{P} - \mathcal{P}M]\,\sigma = 0$$

It is clearly not possible to find a L which satisfies this for all possible states σ; however given

that the first four eigenstates span the possible states of our system to a good approximation, we instead require that it holds on the subspace spanned by these states. We therefore require $[L\mathcal{P} - \mathcal{P}M]\,\sigma_i = 0$ and so $[L - \lambda_i \mathbb{I}]\,(\mathcal{P}\sigma_i) = 0$ for $i = 1, 2, 3, 4$, where σ_i (λ_i) is the i^{th} eigenvector (eigenvalue) of M. So we see that the condition can be satisfied exactly if we require that L would have eigenvectors $\{\mathcal{P}\sigma_i \mid i = 1, 2, 3, 4\}$ with corresponding eigenvalues $\{\lambda_i \mid i = 1, 2, 3, 4\}$. Since there are four eigenvector/eigenvalue pairs, this completely determines L. Performing the calculation one finds,

$$)L\,(\Gamma) = \; L_0 + \Delta\Gamma L_1 + \mathcal{O}\left(\Delta\Gamma^2\right)\,, \tag{S3}$$

where,

$$L_0 = \begin{bmatrix} -0.05 & 0 & 0 & 0.97 \\ 0 & -0.22 & 0 & 0.36 \\ 0 & 0 & -0.22 & 0.36 \\ 0.05 & 0.22 & 0.22 & -1.71 \end{bmatrix}, \quad \text{and} \quad L_1 = \begin{bmatrix} -0.11 & 0 & 0 & -0.01 \\ 0 & -0.45 & 0 & 0 \\ 0 & 0 & -0.45 & 0 \\ 0.11 & 0.45 & 0.45 & 0 \end{bmatrix}.$$

The operator L generated in this way is very close to being population conserving for small Γ, but not exactly so, since some population can be transferred to the excited state manifold. Thus we simply calculate L as above, and then manually impose population conservation, modifying it by the minimal amount required to obtain the thermal evolution L that we seek.

We now consider what thermal reservoirs and couplings this matrix corresponds to. First notice that all the couplings are between the ground states and the singlet, with no couplings between states within the ground state triplet. Also, because the energy difference between the ground state manifold and the singlet is much greater than the differences within the ground state manifold, we can treat the effective temperature and coupling between the $|\pm 1\rangle$ states and the singlet as being the same. Further, by examining the ratios of the rates, we see that the effective temperature between the singlet and $|0\rangle$ is less than that between the singlet and $|\pm 1\rangle$. So we are left with the picture in Fig. S7.

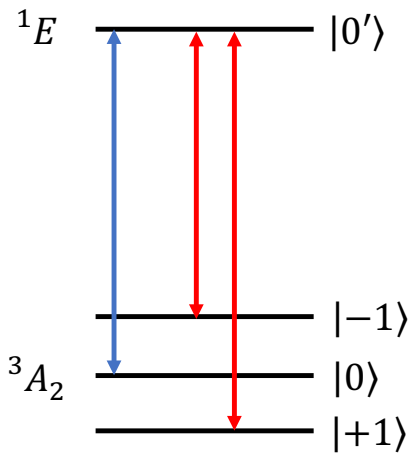

FIG. S7: Schematic description of the effective thermal interaction generated by the optical excitation of the NV^-. Red (blue) arrows represent hot (cold) heat-bath coupling.

Fig. S8 presents the effective thermal excitation rates due to the hot (red) and cold (blue) emulated heat-baths as a function of the optical excitation rate. The emulated thermal decay rates are fixed at 0.97 MHz and 0.36 MHz for the cold and hot baths, respectively (see Eq. S3). The total thermal action is the sum of the excitation and decay rates of both baths, and for the optical excitation rate of 0.76 MHz that was used in the experiment, it amounts to 1.76 MHz.

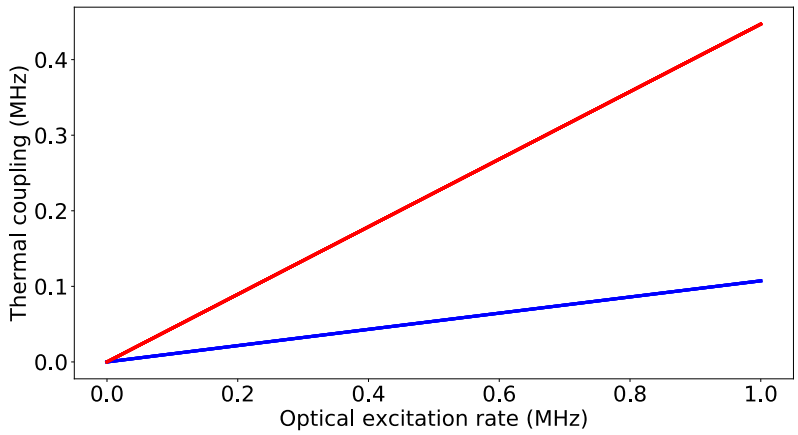

FIG. S8: Effective thermal excitation rates in the emulated thermal action as a function of optical excitation rate. Red (blue) line presents the rate for the hot (cold) bath.

To demonstrate that this is a valid description, consider Fig. S9, which contains a plot of

$\|[L\mathcal{P} - \mathcal{P}M]\,\sigma_0\|$ as a function of evolution time and Γ, for a starting state σ_0 with equal populations in each of the ground and singlet states and $\approx 0.5\%$ in the excited state manifold.

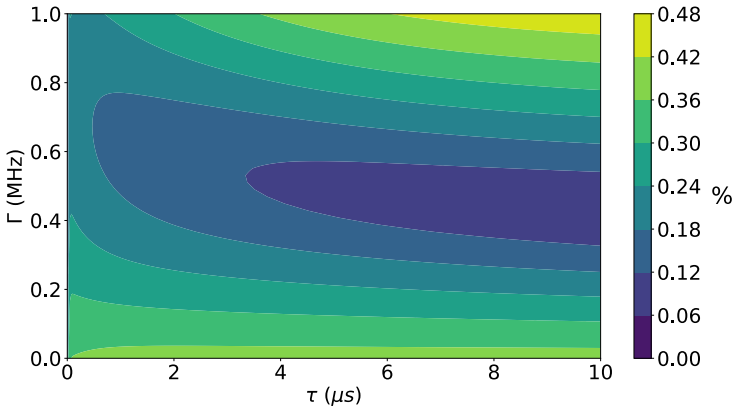

FIG. S9: Difference in state evolution when using the full optical cycle as opposed to the effective thermal interaction. The horizontal (vertical) axis shows the evolution time (optical excitation rate). The scale is the percentage difference in total population.

We can see that the difference between the two descriptions remains below 0.5% for the range of Γ under consideration. We can further consider how the performance of the engine (see Sec. S7) compares when described by the full optical matrix as opposed to the emulated thermal interaction. This is shown in Fig. S10, and here too, the differences are very small within the parameter space used in the experiment.

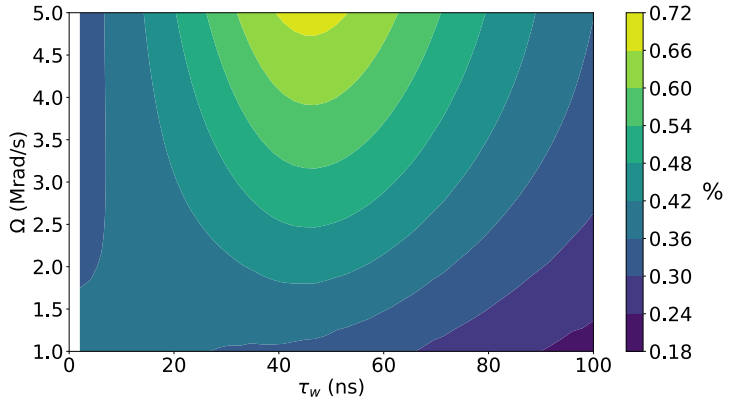

FIG. S10: Difference between the two-stroke engine power output when using the full optical cycle as opposed to the effective thermal interaction. The horizontal (vertical) axis shows the work stroke duration (Rabi frequency). The parameters used are duty-cycle of d = 1/3, $\Gamma = 0.5$ MHz and an inhomogeneous broadening of $2\pi \times 3.0$ MHz. The scale is the percentage difference.

Implementing the baths in this manner has a number of advantages to using real baths. First, whilst the system bath coupling rates, which dictate the thermalisation time of the system, are required to be small, the thermalisation of the bath is set by the phononic decay time from the phonon sideband to the excited state manifold. Due to the rapidity of these decys (< 1 ps), the bath relaxation time is virtually instantaneous compared to the time scales on which the engine operates. In a sense this provides an ideal bath, and we do not need to worry about coarse graining in the Markov approximation. The baths are also ideal in the sense that the bath couplings are independent of driving within the system – this is because the couplings are determined by the optical rates, which are on a much larger energy scale than any shifts due microwave driving.

S7. ENGINE PERFORMANCE CALCULATIONS

The evolution of the engine in contact with thermal reservoirs and an external field is governed by the Lindblad equation [9–11],

$$\hbar\partial_t\rho = -i\left[H_I, \rho\right] + \sum_k A_k \rho A_k^\dagger - \frac{1}{2}\left\{A_k^\dagger A_k, \rho\right\},$$

where H_I is the interaction Hamiltonian which generates unitary evolution, and A_k describes the interaction with thermal baths. We can cast this into matrix operator form by vectorising the density matrix, $\rho \to |\rho\rangle$.

$$\hbar\partial_t |\rho\rangle = \mathcal{H} |\rho\rangle \equiv (-i\mathcal{H}_w + \mathcal{L}) |\rho\rangle ,$$

$\mathcal{H}_w$ results from H_I and is Hermitian, and $\mathcal{L}$ results from the remaining terms and is non-Hermitian. This formalism is known as the Liouville space (or superoperator) formalism. We can write $\mathcal{L} = \mathcal{L}_{coh} \oplus \mathcal{L}_{pop}$, where $\mathcal{L}_{pop\,(coh)}$ is the restriction of $\mathcal{L}$ to the population (coherence) subspace. In our case, we can either take $\mathcal{L}_{pop}$ to be the full rate matrix M, or the effective thermal operator L derived in the previous section. We only have to consider the coherences ρ_{01} and ρ_{10} (as the MW field only couples to the $0 \leftrightarrow 1$ transition), so that $\mathcal{L}_{coh} = -\Gamma\, \mathbb{I}_{2\times 2}$. The restriction of $\mathcal{H}_w$ to the basis $\{\rho_{01}, \rho_{10}, \rho_{00}, \rho_{11}\}$, is given by,

$$\mathcal{H}_w (\Omega, \delta) = \frac{1}{2} \begin{bmatrix} -2\delta & 0 & -\Omega & \Omega \\ 0 & 2\delta & \Omega & -\Omega \\ -\Omega & \Omega & 0 & 0 \\ \Omega & -\Omega & 0 & 0 \end{bmatrix},$$

where Ω is the Rabi frequency, and δ is the detuning of the MW radiation from resonance (resulting from the inhomogeneously broadened ensemble) .

Let $|\,\rho_0(\delta)\rangle$ be the steady state for a given detuning. It is given by the normalised zero eigenstate of the unitary evolution operator for a full two-stroke cycle,

$$U = e^{-i\tau_{th}\mathcal{H}_2} e^{-i\tau_w \mathcal{H}_1},$$

where $\mathcal{H}_1 = \mathcal{H}_w(\Omega, \delta)$, $\mathcal{H}_2 = i\mathcal{L}(\Gamma) + \mathcal{H}_w (0, \delta)$, τ_w is the work stroke duration, and τ_{th} is the thermal stroke duration. The work produced is then simply given by,

$$W (\delta) = \langle H_0 |\, e^{-i\mathcal{H}_1 t_w} - \mathbb{I}\,|\, \rho_0 (\delta)\rangle ,$$

where $|H_0\rangle$ is the vectorised system Hamiltonian ($H_0 = \text{diag}\,[0, \omega_{10}, \omega_{12}]$ and vectorising is achieved by reorganising the elements of H_0 into a column vector) and we have used the identity,

$\langle \mathcal{O} \rangle = \mathrm{Tr}\left(\mathcal{O}\rho\right) = \langle \mathcal{O} \left| \rho \right\rangle$. The total average output power from the ensemble is then found by integrating this over the inhomogeneous distribution, $\mathcal{N}(\delta)$, and dividing by the cycle time, τ_{cyc},

$$\langle P \rangle = \frac{1}{\tau_{cyc}} \int d\delta \; W(\delta) \mathcal{N}(\delta).$$

The detuning distribution was deduced using a Gaussian fit to the measured MW spectrum.

In the above treatment we neglected homogeneous dephasing. The main source of such a process in dense NV ensembles is spin-spin interactions between NV centres (and other paramagnetic impurities) [12]. Its timescale is given by [12], $T_2 \approx 1/\alpha n$, where $\alpha = \mu_0 g_s^2 \mu_B^2 / 4\pi\hbar$ and n is the density of NV centres. Substituting $n = 10^{18} cm^{-3}$ gives $T_2 \approx 2$ μs, which is greater than the longest cycle time used in this work (180 ns) and the inhomogeneous dephasing time due to the inhomogeneous energy distribution $\mathcal{N}(\delta)$ (75 ns), allowing us to safely neglect it.

S8. DERIVATION OF THE STOCHASTIC BOUND

The existence of a stochastic bound was derived in Ref. 1. Here we will present a brief overview of this derivation, together with a description of how the bound was calculated for our case. Such a bound must be independent of the state of a system and should also have no dependence on coherences in the system. As above we start by considering the work produced in a single cycle of the engine; however now with the coherences eliminated at the beginning and end of the cycle,

$$W = \langle H_0 | \, \mathcal{D} \left(e^{-i\mathcal{H}_w t_w} - \mathbb{I} \right) \mathcal{D} \, | \, \rho_0 \rangle \, ,$$

where $\mathcal{D}$ is a projection onto the population subspace (physically it represents a complete dephasing operation), and we include the detuning implicitly. It can be shown [1] that when one expands this expression for small actions, $s \ll \hbar$, one is left with,

$$W = \frac{\tau_w^2}{8} \langle H_0 | \, \mathcal{H}_w^2 \, | \, \rho_{\mathrm{pop}} \rangle + \mathcal{O}\left[(s/\hbar)^4 \right] ,$$

where τ_w is the work stroke duration, and $|\,\rho_{\text{pop}}\rangle \equiv \mathcal{D}\,|\,\rho_0\rangle$. At this point we can simply use the known form of our Hamiltonian to show that,

$$W_{stoch} = \frac{1}{4}\tau_w^2\Omega^2\left[0, \omega_{10}, \omega_{10'}\right]\begin{bmatrix} 1 & -1 & 0 \\ -1 & 1 & 0 \\ 0 & 0 & 0 \end{bmatrix}\begin{bmatrix} \rho_{11} \\ \rho_{00} \\ \rho_{0'0'} \end{bmatrix}$$

$$= \frac{1}{4}\omega_{10}\tau_w^2\Omega^2\left(\rho_{00} - \rho_{11}\right) \leq \frac{1}{4}\omega_{10}\tau_w^2\Omega^2.$$

Then finally the average power is given by,

$$P_{stoch} = W_{stoch}/\tau_{cyc} \leq \frac{1}{4}\omega_{10}d^2\Omega^2\tau_{cyc},$$

where d is the duty cycle.

S9. QUANTUM HEAT ENGINE EQUIVALENCE

This result relates to thermodynamic equivalence of different engine varieties in the small action limit. We begin by considering the three fundamental engine types: continuous, two-stroke, and four-stroke. This result is reached by showing that each of the different stroke varieties is equivalent to the continuous engine as the action tends toward zero. Recall that strokes are simply given by evolution operators of the form $\exp\left(\mathcal{A}t\right)$, with the total cycle evolution being products of such operators. The result relies on the ability to decompose the exponential of a sum into a product of operators. If we were dealing with numbers (or any abelian set) then this occurs trivially since we have, $\exp\left(a+b\right) = \exp\left(a\right)\exp\left(b\right)$ if $[a,b] = 0$. However, because operators do not commute in general, we use a decomposition known as the Strang decomposition (see Refs. 1 and 13),

$$e^{t(X+Y)} = e^{\frac{1}{2}tY}e^{tX}e^{\frac{1}{2}tY} + \mathcal{O}\left(s^3\right)$$

where $s = \left(\|X\| + \|Y\|\right)t$. $\|X\|$ is the spectral norm of the operator X. For this decomposition to be valid we simply require $s \ll 1$. In this case we write,

$$e^{t(X+Y)} \cong e^{\frac{1}{2}tY} e^{tX} e^{\frac{1}{2}tY}$$

Suppose that we have a two-stroke engine with cycle time τ_{cyc}, unitary evolution generator $\mathcal{H}_w$ and Markovian evolution generator $\mathcal{L}$. Further suppose that we wish to compare this two-stroke engine to a continuous engine. Then evolution of a continuous engine in time τ_{cyc} is given by,

$$\mathcal{K}_{cont} = e^{-\frac{i}{\hbar}(\mathcal{H}_w + \mathcal{L})\tau_{cyc}}$$

We can now can apply the Strang decomposition to this operator to obtain,

$$\mathcal{K}_{cont} \cong e^{-\frac{i}{2\hbar}\mathcal{L}\tau_{cyc}} e^{-\frac{i}{\hbar}\mathcal{H}_w\tau_{cyc}} e^{-\frac{i}{2\hbar}\mathcal{L}\tau_{cyc}}$$

Finally, in order to compare this to the two-stroke engine, we need to ensure that the sum of the stroke times in the above decomposition is equal to τ_{cyc}. This is achieved by simply rescaling the couplings,

$$\mathcal{K}_{cont} \cong e^{-\frac{i}{\hbar}\left(\frac{1}{\alpha}\mathcal{L}\right)\left(\frac{\alpha}{2}\tau_{cyc}\right)} e^{-\frac{i}{\hbar}\left(\frac{1}{\beta}\mathcal{H}_w\right)(\beta\tau_{cyc})} e^{-\frac{i}{\hbar}\left(\frac{1}{\alpha}\mathcal{L}\right)\left(\frac{\alpha}{2}\tau_{cyc}\right)},$$

where $\alpha + \beta = 1$. Finally, because this operator is applied repeatedly, cyclic rotations of these operators produce equivalent engines, so we can write,

$$\mathcal{K}_{cont} \cong e^{-\frac{i}{\hbar}\left(\frac{1}{\alpha}\mathcal{L}\right)(\alpha\tau_{cyc})} e^{-\frac{i}{\hbar}\left(\frac{1}{\beta}\mathcal{H}_w\right)(\beta\tau_{cyc})}$$

We can identify β as the duty cycle ($d = \tau_w/\tau_{cyc}$) of the engine. Thus we can see that the two stroke engine with duty cycle d is equivalent to a continuous engine with thermal and unitary operators given by $(1-d)\,\mathcal{L}$ and $d\,\mathcal{H}_w$ respectively. It is possible to continue splitting up these exponentials in an analogous manner to obtain different engine types, including the four-stroke by separating out the hot and cold couplings.

This result shows the dynamical equivalence of these different engine types at the end of each cycle. This implies that these engines will have the same steady states, and will also share the same transient behaviour in their approach to steady state operation. It does not say anything about the

dynamics within the stroke, which might differ significantly – thus the engines are still distinct. This also means that the dynamical equivalence does not immediately imply a thermodynamic equivalence between the different engine types, since work and heat are not state variables. Nevertheless, the equivalence of the net heat and work flows of the different engine types can be shown to be equivalent up to $\mathcal{O}(s^3)$ using a result called the symmetric rearrangement theorem, which was presented and proved in Ref. 1. This states that, if we have time-symmetric couplings $\Omega(t)$, $\gamma_c(t)$ and $\gamma_h(t)$, the heats and work flows into the system are left invariant (up to $\mathcal{O}(s^3)$) under any transformation of these couplings which leaves them time symmetric and their time integrals unchanged.

It can be seen that any Strang splitting of the continuous engine satisfies the conditions for the symmetric rearrangement theorem, which immediately implies that the heat and work flows of the continuous, two-stroke and four-stroke engines are equal provided the action is sufficiently small. It was shown in Ref. 1 that in general the work and heat per cycle differ by $\mathcal{O}(s^1)$ between the different engine types. It is the introduction of coherence which ensures the equivalence up to $\mathcal{O}(s^3)$ for the relevent thermodynamic quantities, showing that this too is a coherence effect.

S10. LINKING THE FLUORESCENCE TO THE ENGINE WORK OUTPUT

In this section we derive the relation between the fluorescence change and the power output of the engine, which is based on the ODMR technique frequently used in NV-centre physics. Although we monitor the fluorescence continuously, the measurement only occurs when a fluorcence photon is emitted, which only occurs during the thermal part of the cycle. Therefore any decoherence due to measurement is already accounted for by decoherence due to the thermal interaction.

As before, let σ be the column vector whose elements represent the populations in the various levels and let M be the optical matrix. Then given some rate, $R(t)$, at which population is transferred from the $|0\rangle$ to the $|1\rangle$ ground states, due to the microwave field, the equation describing the system is,

$$\partial_t \sigma = M\sigma + R(t)\nu, \tag{S4}$$

where $\nu = (-1\ 1\ 0 \cdots 0\ 0)^T$. The rate R is the quantity we wish to determine from the experimentally measured fluorescence. We proceed by considering how the inhomogeneous solution differs from the homogeneous solution (physically the difference between MW driving and no driving).

Let $\Phi(t)$ be the fundamental matrix solution to the homogeneous version of Eq. S4 (that is, a matrix which satisfies $(\partial_t - M)\Phi = 0$). Then it can be checked that the following is a solution to the inhomogeneous equation S4,

$$\sigma(t) = \Phi(t,0)\sigma_0 + \int_0^t d\tau\ \Phi(t,\tau)R(\tau)\nu, \tag{S5}$$

where $\Phi(t,\tau) = \Phi(t)\Phi(\tau)^{-1}$. Once past the transient period, one can take $R(t)$ to be periodic with the same period, τ_{cyc}, as that of $M(t)$, as the microwaves are pulsed at the same rate as the laser pulses. This follows quite generally from Floquet theory and physical considerations. To proceed we need to find the state at the start of the cycle, σ_0 , during this steady state operation. Using the periodicity of the solution we have,

$$\sigma_0 = \sigma(\tau_{cyc}) = \Phi(\tau_{cyc},0)\sigma_0 + \int_0^{\tau_{cyc}} d\tau\ \Phi(\tau_{cyc},\tau)R(\tau)\nu,$$

and therefore,

$$\left[\mathbb{I} - \Phi(\tau_{cyc},0)\right]\sigma_0 = \int_0^{\tau_{cyc}} d\tau\Phi(\tau_{cyc},\tau)R(\tau)\nu. \tag{S6}$$

We would like to solve for σ_0, however the matrix on the left hand side is singular. Note that $\Phi(\tau_{cyc})$ is diagonalisable [it has an inverse: $\Phi(-\tau_{cyc})$], which allows us to write $(\mathbb{I} - \Phi(\tau_{cyc})) = UDU^{-1}$, where D is diagonal. We define the pseudo-inverse, $(\mathbb{I} - \Phi(\tau_{cyc}))^- = UD^-U^\dagger$, where the diagonal matrix D^- is given by:

$$D^-_{ii} = \begin{cases} 1/D_{ii} & \text{if } D_{ii} \neq 0 \\ 0 & \text{otherwise} \end{cases}$$

Let $\mathcal{A} = (\mathbb{I} - \Phi(\tau_{cyc}))^-$. A solution to Eq. S6 is then given by:

$$\tilde{\sigma}_0 = \mathcal{A}\int_0^{\tau_{cyc}} d\tau\ \Phi(\tau_{cyc},\tau)R(\tau)\nu.$$

The full space of solutions to Eq. S4 is then generated by $\alpha\rho_0 + \tilde{\sigma}_0$ for $\alpha \in \mathbb{R}$, where ρ_0 is the (unique) eigenvector of $\Phi(\tau_{cyc})$ with eigenvalue 1. We now show that $\sum_j [\tilde{\sigma}_0]_j = 0$: Suppose $\{\rho_i\}$

are the eigenvectors of $\Phi(\tau_{cyc})$ with corresponding eigenvalues $\{\lambda_i\}$. Then by virtue of $\Phi(\tau_{cyc})$ being population preserving we have,

$$\sum_j \left[\Phi(\tau_{cyc})\rho_i\right]_j = \lambda_i \sum_j \left[\rho_i\right]_j = \sum_j \left[\rho_i\right]_j ,$$

which implies $\sum \left[\rho_i\right]_j = 0$ for $i \geq 1$. Then given a vector ω, $\sum_j \omega_j = 0 \implies \omega \in \text{span}\,(\rho_1, \ldots, \rho_n)$. It is also clear that $\text{Im}\,(\mathcal{A}) \subseteq \text{span}\,(\rho_1, \ldots, \rho_n)$. The unique normalised solution, σ_0, to Eq. S6 is therefore simply obtained by setting $\alpha = 1$ (assuming we have normalised ρ_0). Substituting this back into Eq. S5, we have,

$$\sigma(t) = \Phi(t,0)\rho_0 + \Phi(t,0)\ \mathcal{A}\int_0^{\tau_{cyc}} d\tau\ R(\tau)\Phi(\tau_{cyc},\tau)\vec{\nu} + \int_0^t d\tau\ R(\tau)\,\Phi(t,\tau)\nu$$

and therefore,

$$\sigma(t) - \rho(t) = \Phi(t,0)\ \mathcal{A}\int_0^{\tau_{cyc}} d\tau\ R(\tau)\Phi(\tau_{cyc},\tau)\vec{\nu} + \int_0^t d\tau\ \Phi(t,\tau)R(\tau)\nu,$$

where $\rho(t) = \Phi(t,0)\rho_0$ is the state evolution when $R = 0$. We define the excited state population projector to be the vector $\Omega_E = (0,0,0,1,1,1,0)$, so that the fluorescence rate, $F(t)$, from a state $\sigma(t)$ is proportional to $\Omega_E \cdot \sigma(t)$, where ζ is the radiative decay rate. Denote the time dependent fluorescence in the presence of MW driving by $F(t)$ and denote the fluorescence in the absence of MW driving by $F_0(t)$. Further define,

$$g(t,\tau) = \Omega_E \cdot \Phi(t,0)\ \mathcal{A}\ \Phi(\tau_{cyc},\tau)\cdot\nu \quad \text{and} \quad f(t,\tau) = \Omega_E \cdot \Phi(t,\tau)\cdot\nu.$$

We can then write,

$$\left[\frac{1}{\langle F_0\rangle\,\tau_{cyc}}\int_0^{\tau_{cyc}} d\tau\ \Omega_E\cdot\rho(\tau)\right] \times (F(t) - F_0(t)) = \int_0^{\tau_{cyc}} d\tau\ g(t,\tau)R(\tau) + \int_0^t d\tau\ f(t,\tau)R(\tau),$$

where the term in square parenthesis is the proportionality constant linking the fluorescence to the excited state population. This can be written more succinctly as,

$$\left[\frac{1}{\tau_{cyc}}\int_0^{\tau_{cyc}} d\tau\ \Omega_E\cdot\rho(\tau)\right] \times \frac{\Delta F(t)}{\langle F_0\rangle} = \int_0^{\tau_{cyc}} d\tau\ h(t,\tau)R(\tau),$$

where we have defined $\Delta F(t) = F(t) - F_0(t)$, and

$$h(t,\tau) = \begin{cases} g(t,\tau) + f(t,\tau) & \text{if } t > \tau \\ g(t,\tau) & \text{otherwise.} \end{cases}$$

Experimentally, we only measure the change in the *average* fluorescence, $\langle \Delta F \rangle$, so we must integrate t over the period to obtain,

$$\left[\frac{1}{\tau_{cyc}}\int_0^{\tau_{cyc}} d\tau\ \Omega_E \cdot \rho(\tau)\right] \times \frac{\langle \Delta F \rangle}{\langle F_0 \rangle} = \frac{1}{\tau_{cyc}}\int_0^{\tau_{cyc}} d\tau\ H(\tau)R(\tau),$$

where $H(\tau) = \int_0^{\tau_{cyc}} dt\, h(t,\tau)$. It can be shown numerically that, for sufficiently small cycle duration and optical pumping rate, H is constant to a good approximation (for the maximum stroke duration and optical intensity used in the experiment, the relative change of H over the interval is $\sim 4 \times 10^{-4}$). This allows us to write,

$$\langle R \rangle = \kappa(\Gamma)\frac{\langle \Delta F \rangle}{\langle F_0 \rangle}, \tag{S7}$$

where

$$\kappa(\Gamma) = \frac{1}{H\tau_{cyc}}\int_0^{\tau_{cyc}} d\tau\ \Omega_E \cdot \rho(\tau).$$

Note that $\kappa(\Gamma)$ does not depend on the MW driving, but only on the optical pumping rate, Γ, and the known decay rates of the system. Fig. S11 presents κ vs. the optical excitation rate Γ for both continuous and two-stroke engines, for the range of optical excitation rates used in the experiment. The error (one standard deviation) in the value of κ, estimated using the Monte-Carlo method, is presented by the shaded areas.

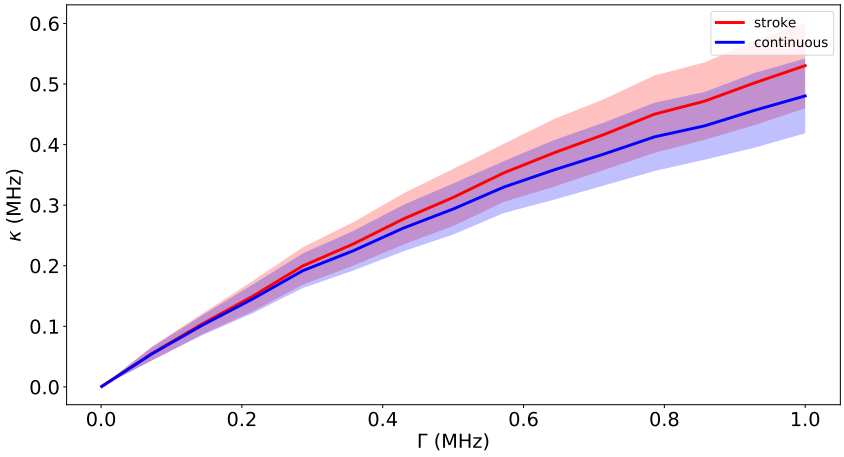

FIG. S11: $\kappa(\Gamma)$ for a continuous engine (red), and two-stroke engine with a duty cycle of $d = 1/3$ (blue). The shaded areas represent the error in κ (one standard deviation).

The average power is then simply given by,

$$\langle P \rangle = \hbar\omega_{10} \langle R \rangle = \hbar\omega_{10}\kappa \left(\Gamma\right) \frac{\langle \Delta F \rangle}{\langle F_0 \rangle}, \tag{S8}$$

where $\hbar\omega_{10}$ is the energy gap between the relevant levels.

S11. UNCERTAINTY ANALYSIS

In examining expression S8 it is apparent that there are a number of contributions to the uncertainty in the final value of the power, $\langle P \rangle$. There is measurement variation in the value $\langle \Delta F \rangle$ from one measurement to the next, due to detector shot noise. The mean and standard error were simply calculated from a sample of individual measurements. The value for κ depends on the parameters listed in table S1, together with the value calculated for Γ, which itself depends on the former parameters. We use a Monte-Carlo simulation to propagate the uncertainties in these parameters, and the calculated uncertainty for Γ, to a final uncertainty in κ. The error in the value for $\langle F_0 \rangle$ was determined to be negligible (relative error $< 1\%$) relative to the other errors and therefore disregarded. Finally we also need to account for uncertainty in the value for the bound. This stems principally from the uncertainty in the value for the Rabi frequency.

The quantity of interest is the certainty with which we can demonstrate $P_{measured} - P_{bound} > 0$. This requires that we use a one sided normal distribution. The null hypothesis is $P_{measured} - P_{bound} \leq 0$, whilst the alternative hypothesis is that the measured power breaks the stochastic bound. In our case the test statistics for the null outcome is $t = 2.4$, which corresponds to a p-value of 0.0082. Thus we can discard our null hypothesis and adopt the alternative hypothesis, to a significance of $< 1\%$.

[1] R. Uzdin, A. Levy, and R. Kosloff, Phys. Rev. X **5**, 031044 (2015).

[2] J. Tetienne, L. Rondin, P. Spinicelli, M. Chipaux, T.Debuisschert, J. Roch, and V.Jacques, New J. Phys. **14**, 103033 (2012).

[3] T.-L. Wee, Y.-K. Tzeng, C.-C. Han, H.-C. Chang, W. Fann, J.-H. Hsu, K.-M. Chen, and Y.-C. Yu, J. Phys. Chem. A **111**, 9379 (2007).

[4] M. W. Doherty, N. B. Manson, P. Delaney, F. Jelezko, J. Wrachtrup, and L. C. L. Hollenberg, Phys. Rep. **528**, 1 (2013).

[5] N. Aslam, G. Waldherr, P. Neumann, F. Jelezko, and J. Wrachtrup, New Jurnal of Physics **15**, 013064 (2013).

[6] J. Rogers, R. McMurtrie, M. Sellars, and N. Manson, New J. Phys. **11**, 063007 (2009).

[7] M. Doherty, N. Manson, P. Delaney, and L. Hollenberg, New J. Phys. **13**, 025019 (2011).

[8] M. L. Goldman, A. Sipahigil, N. Y. Yao, S. D. Bennett, N. B. Manson, A. Kubanek, and M. D. Lukin, Phys. Rev. B **91**, 165201 (2015).

[9] H.-P. Breuer and F. Petruccione, *Open quantum systems* (Oxford university press, 2002).

[10] G. Lindblad, Communications in Mathematical Physics **48**, 119 (1976).

[11] V. Gorini and A. Kossakowski, J. Math. Phys. **17**, 1298 (1976).

[12] J. M. Taylor, P. Cappellaro, L. Childress, L. Jiang, D. Budker, P. R. Hemmer, A. Yacoby, R. Walsworth, and M. D. Lukin, Nature Physics **4**, 810 (2008).

[13] T. Jahnke and C. Lubich, BIT Numerical Mathematics **40**, 735 (2000).